Closed-loop High-fidelity Simulation Integrating Finite Element Modeling with Feedback Controls in Additive Manufacturing

Dan Wang
Dept. of Mechanical Engineering
University of Washington
Seattle, Washington, 98195
Email: daw1230@uw.edu

Xu Chen*
Dept. of Mechanical Engineering
University of Washington
Seattle, Washington, 98195
Email: chx@uw.edu

A high-precision additive manufacturing process, powder bed fusion (PBF) has enabled unmatched agile manufacturing of a wide range of products from engine components to medical implants. While finite element modeling and closed-loop control have been identified key for predicting and engineering part qualities in PBF, existing results in each realm are developed in opposite computational architectures wildly different in time scale. This paper builds a first-instance closed-loop simulation framework by integrating high-fidelity finite element modeling with feedback controls originally developed for general mechatronics systems. By utilizing the output signals (e.g., melt pool width) retrieved from the finite element model (FEM) to update directly the control signals (e.g., laser power) sent to the model, the proposed closed-loop framework enables testing the limits of advanced controls in PBF and surveying the parameter space fully to generate more predictable part qualities. Along the course of formulating the framework, we verify the FEM by comparing its results with experimental and analytical solutions and then use the FEM to understand the melt-pool evolution induced by the in- and cross-layer thermomechanical interactions. From there, we build a repetitive control algorithm to attenuate variations of the melt pool width.

1 Introduction

Distinct from conventional subtractive machining, additive manufacturing (AM) builds a part directly from its digital model by joining materials layer by layer. In particular, applying high-precision lasers or electron beams as the energy source, powder bed fusion (PBF) AM has enabled unprecedented fabrication of complex parts from polymeric and metallic powder materials. However, broader adoption of the technology remains challenged by insufficient reliability and in-process variations. These variations are induced by, for example, uncertain laser-material interactions, environmental vibrations, powder recycling, imperfect interactions of mechanical components, and complex thermal histories of materials [1–3].

PBF builds a typical part from many thousands of thin layers. Within each layer (Fig. 1), the energy beam is regulated to follow trajectories predefined by the part geometry in a slicing process. After the printing of one layer, a recoater will spread a new thin layer of powder over the just-fused layer, and then another cycle will begin. Current researches employ finite element modeling and feedback controls to understand the energy-deposition mechanisms and to regulate the in-process variations in PBF. For instance, [4–7] adopt finite element modeling to investigate how various scan patterns, scan speeds, number of lasers, overhanging structures, and underlying physics affect the thermal fields of the powder bed, the geometries of the melt pool, and the mechanical properties of the printed parts. Specially, [8] brings up the idea of building digital twins of AM machines by integrating various high-fidelity multiphysics models. Existing feedback control strategies usually implement low-order system models obtained from system identification techniques, such as [2, 9, 10] in PBF and [11–13] in laser metal deposition (LMD), an AM technology analogous to PBF. A nonlinear memoryless submodel [12, 14] and a spatial-domain Hammerstein model [13] are further built in LMD to cover more complicated process dynamics. From there, PID control, sliding mode control, predictive control, and iterative learning control have proved their efficiencies in improving the dimensional accuracy of the printed parts in PBF [2,9,15,16] and in LMD [11, 14, 17–20].

Although finite element model (FEM) and feedback control have been identified key for predicting and engineering part qualities in PBF, existing results in each realm are developed in separate computational architectures due to their different time scales. Feedback controls are implemented in real time, while FEM takes hours or even days to simulate the printing of a few layers that finishes in seconds in reality. If we can integrate FEM with feedback controls directly in a closed loop, however, we can 1) combine afore-

*Corresponding author

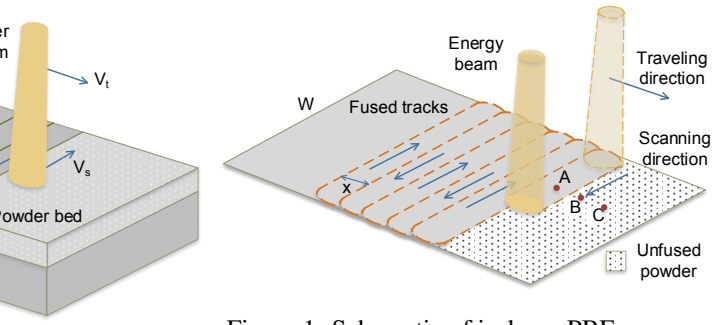

Figure 1: Schematic of in-layer PBF process.

mentioned knowledge from each realm, 2) test the limit of advanced control in PBF, 3) survey the parameter space fully to generate more predictable part qualities, and 4) quickly design controllers and update parameters for novel materials and printer settings. These benefits are more prominent when the experiments are costly and time-consuming.

In pursuit of the above benefits, this paper builds, in the first instance to our best knowledge, a closed-loop high-fidelity simulation framework that leverages modern architectures of finite-element-modeling tools and the power of data processing and advanced controls. In particular, we build a bidirectional architecture so that the output signals (e.g., melt pool width or peak temperature) retrieved from the FEM can be utilized to directly update the FEM process parameters (e.g., laser power or scan speed) in external control toolboxes (e.g., MATLAB). In this way, we design an interface that enables simulating closed-loop controllers for PBF thermal processes. Along the course of formulating the framework, we validate the FEM by comparing its results with experimental and analytical solutions and then use the verified FEM to investigate the periodic in- and cross-layer thermal interactions. From there, we justify the effectiveness of the repetitive control (RC) in attenuating the periodic variations of the melt pool width.

The major contributions of this paper are:

- developing a closed-loop simulation architecture for implementing and testing out feedback control strategies in FEM;
- building an RC algorithm and an FEM of the PBF thermal process, as applications of the proposed architecture;
- verifying the effectiveness of RC in regulating the periodic thermal interactions in PBF.

The remainder of this paper is structured as follows. Section 2 frames the main closed-loop high-fidelity simulation with the bidirectional architecture between FEM and controller. As application examples, Section 3 develops an FEM of the thermal fields in PBF, and Section 4 builds an RC design to regulate the periodic thermal cycles. Under the architecture of the closed-loop simulation, Section 5 evaluates the performance of RC. Section 6 concludes the paper.

2 Architecture of Proposed Closed-Loop Simulation with Bidirectional Communication Between FEM and Feedback Controls

We propose in this section the main closed-loop simulation that integrates FEM with feedback controls directly in a closed loop. The key idea is to use the output signals (e.g., melt pool width) retrieved from the FEM to update through the controller the control signals (e.g., laser power) sent back to the FEM. The core of the FEM is the numerical simulation of a partial differential equation (PDE) of the general form:

$$f(x_1,\ldots,x_n;u,\frac{\partial u}{\partial x_1},\ldots,\frac{\partial u}{\partial x_n};\frac{\partial^2 u}{\partial x_1\partial x_1},\ldots,\frac{\partial^2 u}{\partial x_1\partial x_n};\ldots)=0,$$

where u is the output signal predicted by the FEM and $x_1,\ldots,x_n$ are the independent variables. Examples of PDEs in PBF include the governing equations for heat transfer, thermal stress, and fluid flow; the output signals are thereby the temperature, stress, and melt pool velocity, respectively [21, 22]. On the other hand, in feedback control, an output signal is compared with a reference signal to generate an error signal, which is then filtered by a controller to produce a control signal. By reacting to the in-process change of the output signal, feedback control compensates for model inaccuracies and unmeasured disturbances.

Leveraging the power of FEM and feedback controls, we develop the closed-loop simulation algorithm and outline its workflow as follows:

1. Designing and initializing the FEM in an FEM software (e.g., COMSOL) and the controller in a control-oriented scripting programming environment (abbreviated as programming environment, e.g., MATLAB). For the focused closed-loop FEM in this paper, we set the computation time of the FEM as t_s, where t_s is the sampling time of the discrete-time feedback loop;
2. Building an interface to connect the FEM software with the programming environment. This interface enables simulating closed-loop controllers for FEM and taking advantage of the programming environment in preprocessing, model manipulation, statistical analysis, and post-processing;
3. Through the interface, the programming environment retrieves the output signal from the FEM software. Thereafter, the controller processes the output signal to get the new control signal, which is then sent back to the FEM. With the updated control signal, a new FEM computation begins;
4. Repeating step 3 until the whole simulation ends.

With the bidirectional architecture between the FEM and controller, the closed-loop simulation enables updating directly the control signals of the FEM, retrieving signals hard to reach by experiments, and surveying the parameter space fully before real PBF experiments. Moreover, the proposed architecture is agnostic to the types of programming environment and FEM software, facilitating incorporating various control methods into different multiphysics simulations

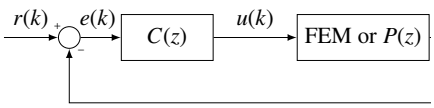

Figure 2: Block diagram of general feedba

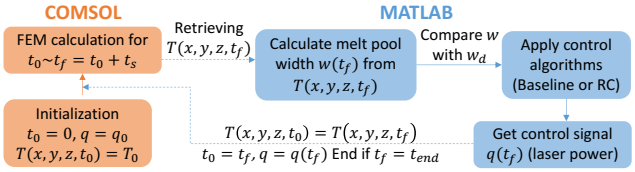

Figure 3: Schematic of proposed closed-loop simulation.

Algorithm Closed-loop simulation

1 Import classes
2 Open the FEM file
3 Initialize parameters of FEM and Controller
  $t_0 = 0$, $t_f = t_0 + t_s$, $T(t_0) = T_0$, $q = q_0$
4 While $t_f \leq t_{end}$:
  1 Call FEM software to compute the FEM
  2 Get the temperature distribution $T(t_f)$
  3 Calculate melt pool width $w(t_f)$ from $T(t_f)$
  4 Apply controller to update laser power $q(t_f)$
  5 Update iterative variables in the FEM
    $t_0 \leftarrow t_f$, $T(t_0) \leftarrow T(t_f)$, $q \leftarrow q(t_f)$

- The computation time of FEM is t_s, where t_s is the sampling time in discrete-time feedback control.

Figure 4: Pseudocode of closed-loop simulation algorithm.

(e.g., heat transfer and fluid flow studies). As amples, we choose COMSOL Multiphysics, *LiveLink for MATLAB* to build the FEM, con terface, respectively. We provide in this sectio of an FEM of the thermal fields and a feedb sign. We will build the detailed FEM and co tions 3 and 4, respectively.

1) The governing equation for the conduction heat flow in PBF is

$$\rho c_p \frac{dT(x,y,z,t)}{dt} = \nabla \cdot (k \nabla T(x,y,z,t)) + q_s, \qquad (1)$$

where k is the thermal conductivity, c_p the specific heat capacity, ρ the effective density, t the time, T the temperature, and q_s the rate of local internal energy generated per unit volume [23]. When no confusion would arise in the context, we abbreviate $T(x,y,z,t)$ to T in the rest of this paper.

The initial condition is defined by setting $T(x,y,z,0)$ as the ambient temperature T_0. When the substrate (Fig. 6) is designed to be large enough compared to the heat-affected zone, one boundary condition is established by assuming the bottom ($z = h$) of the substrate has no heat loss [4–6]: $-k\frac{\partial T}{\partial z}\Big|_{z=h} = 0$. A quantitative way to test and validate the size of the substrate is that from the FEM results, the bottom of the substrate should maintain the temperature of T_0. The other boundary condition is established by considering the top surface ($z = 0$) of the powder bed with input heat flux, convection heat loss, and radiation heat loss:

$$-k\frac{\partial T}{\partial z}\Big|_{z=0} = -Q + h_c(T - T_0) + \varepsilon\sigma_B(T^4 - T_0^4), \qquad (2)$$

where Q is the input heat flux, h_c the convection heat transfer coefficient, ε the emissivity, and σ_B the Stefan-Boltzmann constant. Here, we assume Q has a Gaussian laser beam profile: $Q \approx \frac{2q}{\pi R^2} e^{-\frac{2r^2}{R^2}}$, where q is the laser power, R the effective laser beam radius, and r the radial distance from a certain point to the center of the laser spot. From the temperature distribution predicted by the FEM, melt pool width can be further calculated, as will be elaborated in Section 3.1. From here on, we select melt pool width w as the output signal and laser power q as the control signal for the subsequent feedback control design.

2) A generic feedback system consists of a plant $P(z)$ and a controller $C(z)$ (Fig. 2). In this study, $P(z)$ is the plant model identified from the FEM simulation. The signal $r(k)$ represents the system reference, which here is a desired melt pool width; $u(k)$ represents the control signal, which here is the laser power; $y(k)$ represents the system output, which here is the melt pool width as calculated from FEM-predicted temperature fields; $d(k)$ represents the input disturbance, which here is the in-process melt-pool-width variations.

Fig. 3 demonstrates the operating procedures of the proposed closed-loop simulation architecture, taking as examples the FEM of the PBF thermal process and general feedback control. We design and initialize the FEM in COMSOL while programming in MATLAB the main file of the architecture that includes the interface establishment, the controller design, and the recursive calls for COMSOL. First, we initialize the FEM by setting the start time t_0 as 0, the laser power q as an initial value q_0, and the temperature distribution $T(x,y,z,t_0)$ as the ambient temperature T_0. The computation time of the FEM is set as one time step from t_0 to $t_f = t_0 + t_s$. After the initialization, MATLAB will call COMSOL to start the FEM computation. After retrieving the FEM-predicted temperature distribution $T(x,y,z,t_f)$, the main file in MATLAB calculates the melt pool width $w(t_f)$ from $T(x,y,z,t_f)$ and, based on the control algorithms, processes $w(t_f)$ and its historical values to obtain the control signal $q(t_f)$. After that, the FEM is updated by assigning the iterative variables t_0 as t_f, $T(x,y,z,t_0)$ as $T(x,y,z,t_f)$, and the laser power as $q(t_f)$. After passing all closed-loop computed information, MATLAB will call COMSOL to start the FEM computation with the updated variables, and a new cycle will begin. The closed-loop simulation will stop when t_f reaches to the whole simulation time t_{end} ($\gg t_f$ in general).

We provide in Fig. 4 the pseudocode of the main file in the closed-loop simulation algorithm. After importing the necessary classes for building the FEM, controller, and in-

terface, the algorithm opens the FEM file and initializes the parameters of the FEM and controller. Inside the *while* loop, the main file calls the FEM software to compute the FEM simulation and then retrieves the predicted temperature distribution $T(x, y, z, t_f)$. Based on $T(x, y, z, t_f)$, the algorithm calculates the melt pool width $w(t_f)$ and thereafter processes $w(t_f)$ and its historical values through the controller to get the new laser power. At last, the algorithm updates the iterative variables of the start time, the initial temperature, and the laser power to get prepared for a new iteration. The Appendix provides the main MATLAB commands used in the closed-loop simulation.

The proposed closed-loop simulation establishes not only a bidirectional communication between FEM software and programming environment, but also an interface specifically for the purpose of simulating feedback controllers in FEM. The built architecture will benefit and guide experiments by validating beforehand the effectiveness of the servo designs. Next we will present the detailed FEM and controller designs in Sections 3 and 4, respectively.

3 FEM of Thermal Fields in PBF

In this section, we use the COMSOL Multiphysics 5.3a software to build and refine the FEM of the temperature response in PBF, which serves as an essential component of the proposed closed-loop simulation. We verify the FEM configuration by comparing the numerical results with the experimental and analytical solutions. The FEM developed in this section considers conduction, latent heat of fusion, surface convection, and surface radiation. The principal objective of the paper is not to create a new high-fidelity FEM at microscopic fluid flow level but to develop and test the closed-loop simulation architecture. Therefore, we omit the effects of evaporation, fluid flow, and Marangoni force for easier testing in the general control community. The FEM built in this section is intended as one application example of the proposed architecture between FEM and controller. However, the physics of complex melt flow (e.g., Marangoni and surface tension effects) can be readily added to increase the model accuracy and provide more microscopic details of the melt pool that are beyond the focus of this paper.

3.1 FEM

We have elaborated the governing equation, initial condition, and boundary conditions in Section 2. For the temperature-dependent thermal properties in (1), we adopt k, c_p, and ρ in [4, 24] for the solid and liquid materials, as shown in Fig. 5. We generate the thermal properties of the powder material from those of the solid material by considering the powder-bed porosity ϕ [25, 26]:

$$k_{powder} = k_{solid}(1-\phi)^4 \quad \text{and} \quad \rho_{powder} = \rho_{solid}(1-\phi),$$

Table 1: Parameters of the FEM. Note that the laser spot diameter of 70 µm is for model verification in Section 3.2.

Parameters	Value
Size of powder bed	5 mm × 10 mm × 50 µm
Size of substrate	5 mm × 10 mm × 2 mm
Powder/substrate material	Ti6Al4V
Laser power q	60 W or varying [28]
Scan speed u_x	100 mm/s [28]
Track length L	5 mm
Laser spot diameter $2R$	220 µm (or 70 µm [28])
Ambient/initial temp.	293.15 K
Initial porosity ϕ_0	0.4 [4, 24]
Emissivity	0.35 [4]
Powder bed absorptance	0.25 [4]
Time step t_s	0.5 ms
Melting point T_m	1923.15 K [29]
Solidus temperature T_{sol}	1873 K [29]
Latent heat of fusion L_f	295 kJ/kg [29]
Convection h.t. coeff. h_c	12.7 W/(m^2·K) [4]
k, c_p, and ρ	See Fig. 5 [4, 24–26]

where ϕ is expressed as

$$\phi(T) = \begin{cases} \phi_0 & T_0 < T \le T_{sol} \\ \frac{\phi_0}{T_{sol}-T_m}(T-T_m) & T_{sol} < T < T_m \\ 0 & T \ge T_m \end{cases},$$

with ϕ_0 denoting the initial porosity. Here, the heat capacity is assumed to be the same for the powder and solid materials [25]. Especially, we account for the latent heat of fusion L_f by introducing the effective heat capacity to the powder material [27]:

$$c_{p,eff}(T) = \begin{cases} c_{p1}(T) & T_0 < T \le T_{sol} \\ \frac{L_f}{T_m-T_{sol}} + \frac{c_{p1}(T_{sol})+c_{p2}(T_m)}{2} & T_{sol} < T < T_m \\ c_{p2}(T) & T \ge T_m \end{cases}, \quad (3)$$

where T_0 is the ambient temperature, T_{sol} the solidus temperature, T_m the melting point, c_{p1} the heat capacity of the powder, and c_{p2} the heat capacity of the liquid. Table 1 lists the process parameters used in this study unless otherwise specified. To justify the parameter values, we introduce here the volumetric energy density E_v, which is a key factor in the PBF process and directly impacts on the properties of as-built parts. E_v is defined as: $E_v = P/(vth)$, where P is the laser power, v the laser scan speed, t the layer thickness, and h the hatch spacing [30]. During the in-layer multitrack printing (Sections 4.2 and 5), $P = 60$ W, $v = 100$ mm/s, $t = 50$ µm, and $h = 60$ µm, which gives $E_v = 200\,\text{J/mm}^3$. This volumetric energy density is, for example, in the ranges of $71 \sim 373\,\text{J/mm}^3$ as studied in [31] and $15 \sim 240\,\text{J/mm}^3$ as in [32].

Fig. 6a shows the bidirectional scan scheme used in this study and the whole build with a substrate and a thin layer

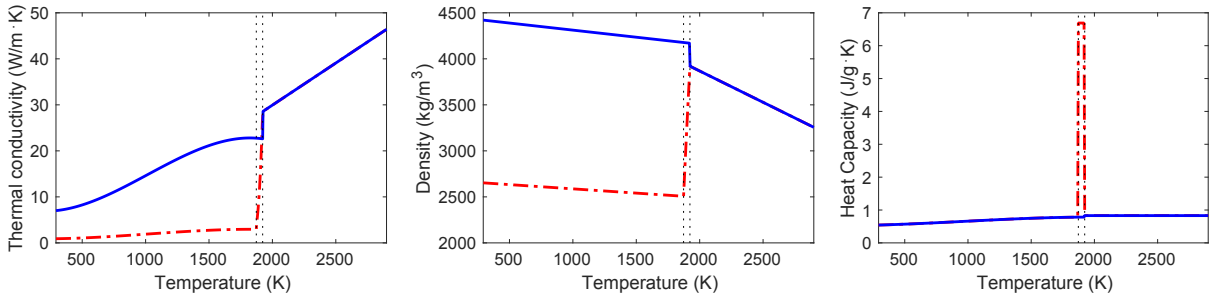

Figure 5: Temperature-dependent thermal properties of Ti6Al4V [4, 24–26]. Solid line: solid and liquid materials. Dash-dotted line: powder material. The two vertical dotted lines respectively indicate T_{sol} and T_m.

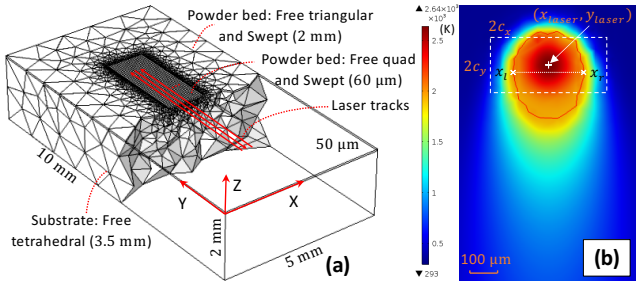

Figure 6: (a): a thin layer of powder bed and the substrate with selective meshing scheme. (b): surface temperature distribution at $t = 0.14$ s. The lined isotherm indicates $T = T_m$.

Algorithm Calculation of Melt Pool Width

1 Locate laser beam position: x_{laser} and y_{laser}

2 Points to traverse:

$$X = \{x_{laser} - c_x : \Delta x : x_{laser} + c_x\}$$
$$Y = \{y_{laser} - c_y : \Delta y : y_{laser} + c_y\}$$

3 for y in Y:

  1 for x in X:

    1 Locate $T(x_l, y) = T_m$ and $T(x_r, y) = T_m$

  2 Width defined by T_m for a certain y:

$$w_y = x_r - x_l$$

4 Melt pool width $w = \max(w_y)$

- In this case study, $\Delta x = \Delta y = 1$ μm, $c_x = 150$ μm, and $c_y = 100$ μm

Figure 7: Pseudocode for calculating melt pool width.

of powder bed. Here, we use a selective meshing scheme to balance model accuracy with computation time: a fine quad-and-swept mesh with a maximum element size of 60 μm is applied to the central powder bed region that directly interacts with the energy beam, whereas less fine tetrahedral mesh (3.5 mm) and triangular-and-swept mesh (2 mm) are applied to the substrate and the peripheral powder bed, respectively. Fig. 6b showcases a surface temperature distribution, where the isotherm of $T = T_m$ indicates the melt pool geometry.

From the FEM-predicted temperature distribution, Fig. 7 shows the pseudocode of how to calculate the melt pool width. The basic principle is to search around the position of the laser beam to find the maximum width of the melt pool bounded by T_m. The first step is to locate the position of the laser beam (x_{laser}, y_{laser}), as shown in Fig. 6b. Then we identify the points to traverse by testing and ensuring that the rectangle $2c_x \times 2c_y$ be inclusive of anticipated melt pool widths (Fig. 6b). A set X stores the x coordinates of these points with an increment Δx, and a set Y stores the y coordinates with Δy. For each y in Y, we search in X to find the left boundary x_l and right boundary x_r that have the temperature of T_m. A width w_y for a certain y is given by $x_r - x_l$. After going over all the points, we identify the melt pool width as the maximum w_y. In this study, we choose $\Delta x = \Delta y = 1$ μm, $c_x = 150$ μm, and $c_y = 100$ μm.

3.2 Model Verification

This section verifies the developed FEM by comparing the numerical melt pool widths with the experimental and analytical solutions. Table 2 first compares the melt pool widths obtained from the developed FEM with the experimental results in [28]. The laser power is fixed to be 50 W, the laser spot diameter is 70 μm, and the scan speed is 100, 200, or 300 mm/s. The FEM gives reasonable predictions of the melt pool widths with errors less than 10%.

Table 2: Melt pool widths from FEM and experimental results [28] with a fixed laser power of 50 W and different scan speeds. Difference (Diff.)=FEM-Experiments (Exper.). Error=|FEM-Exper.|/FEM.

Scan speed	FEM(μm)	Exper. (μm)	Diff. (μm)	Error (%)
100 mm/s	182	165.7~175.4	6.6~16.3	3.6~9.0
200 mm/s	152.6	140.7~142.9	9.7~11.9	6.4~7.8
300 mm/s	132.6	120.7~125.4	7.2~11.9	5.4~9.0

Then we compare the numerical melt pool widths with the analytical solutions. When a moving point laser source is acting on a thick plate and the thermal properties of the plate are constant, the analytical solution of (1) in the steady state is the Rosenthal equation [23]:

$$T(\xi, y, z) - T_0 = \frac{q}{2\pi k r} \mathrm{e}^{-\frac{u_x(r+\xi)}{2\kappa}}, \tag{4}$$

where (ξ, y, z) is a coordinate system attached to the moving laser source, $r = \sqrt{\xi^2 + y^2 + z^2}$, and $\kappa = k/(\rho c_p)$. For comparison, we adapt the FEM to accommodate the assumptions of the Rosenthal equation, such as constant thermal properties ($k = 5$ W/(m·K), $c_p = 1.1$ J/(g·K), and $\rho = 4300$ kg/m^3) and

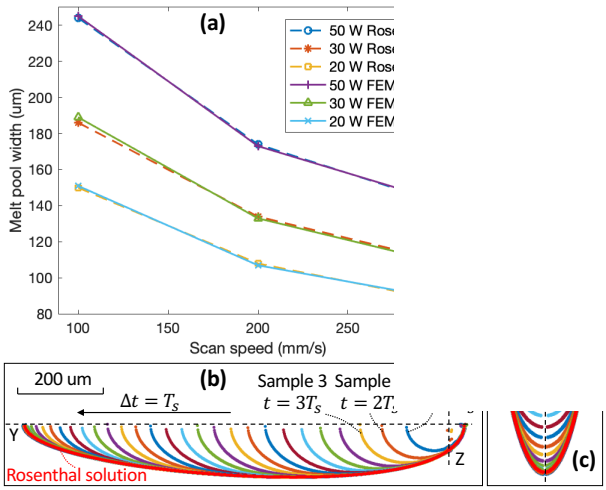

Figure 8: Melt pool widths from the FEM and analytical solutions. (b) and (c) share the same scale and legend.

point heat source. Fig. 8 compares the numerical and analytical solutions. From Fig. 8a, we can tell that the melt pool widths obtained from the FEM and the Rosenthal equation match well with each other under different combinations of scan speeds and laser powers. Also, as shown in Figs. 8b and 8c, after 27 samples, the numerical melt pool geometry reaches to the steady state and matches with the Rosenthal solution (the outline).

4 Repetitive Controller Design

This section looks into another fundamental component of the closed-loop simulation, namely, the controller design. We first adopt the FEM in Section 3 to investigate the periodic PBF thermal cycles and then design a repetitive controller to regulate these cycles.

4.1 Periodic Thermal Interactions: Hatch Spacing

We first examine how hatch spacing affects the melt pool variation, especially during the transition from the end of one track (named P1) to the start of the adjacent track to be sintered (P2). Here, hatch spacing is defined as the distance between two adjacent scan vectors and denoted as Δx in Fig. 1. When the hatch spacing (e.g., 47 µm in (a1)-(a4) of Fig. 9) is much less than half of the melt pool width (around the laser spot radius 110 µm), the laser spot at P2 will be centered inside the melt pool region of P1 and thus can take advantage of the accumulated heat, yielding a well-developed melt pool at 50.5 ms. When the hatch spacing (e.g., 100 µm in (b1)-(b4) of Fig. 9) is close to or larger than half of the melt pool width, the laser spot at P2 will be centered out of the melt pool region of P1, yielding a lower initial temperature at P2. Besides, since the laser is turned off during the transition, a larger hatch spacing (100 µm) gives a longer dwell time (1 ms) with the same scan speed (100 mm/s). Hence, previously fused tracks would have more time to cool down, which also yields a lower initial temperature at P2. Therefore, the melt pool evolves slower at P2, and two immature states show up at 550.5 ms and 551 ms, which will cause more porosity in the printed part.

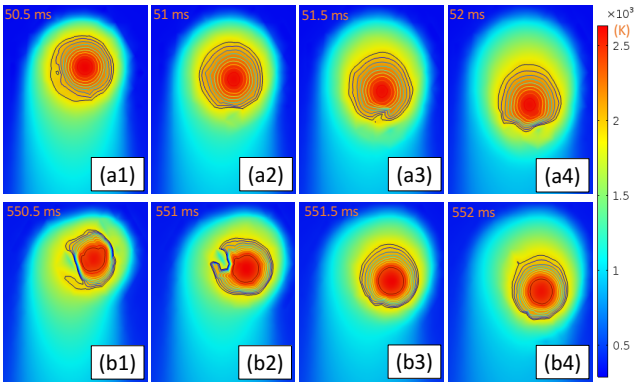

Figure 9: Melt pool variations at the start of the 2nd track with hatch spacing of 47 µm (i.e., dwell time of 0.47 ms) in (a1)-(a4) and the start of the 12th track with hatch spacing of 100 µm (i.e., dwell time of 1 ms) in (b1)-(b4).

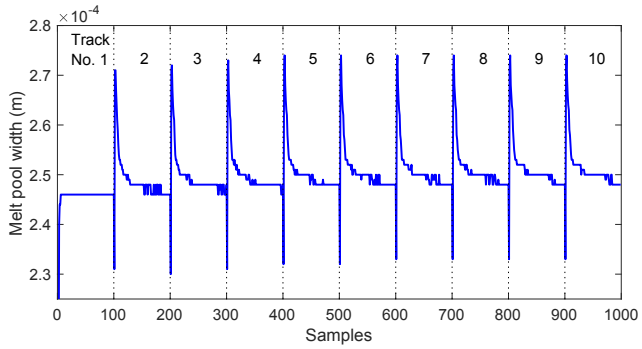

(a) Evolution of melt pool width (time-domain)

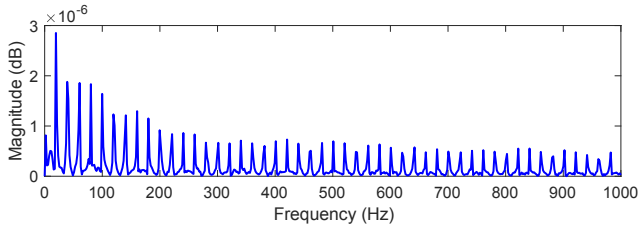

(b) FFT of melt-pool-width evolution (frequency-domain)

Figure 10: In-layer thermal disturbance with constant laser power.

To get consistent part quality in PBF, a stable melt pool is desired during the transition. The immature melt pool states can be eliminated by decreasing the hatch spacing. However, there is a trade-off between melt pool stability and printing efficiency since simply shortening the hatch spacing increases printing time. Next we will study periodic melt pool variations that are intrinsic in the PBF process and demand much more involved solutions, such as advanced control algorithms.

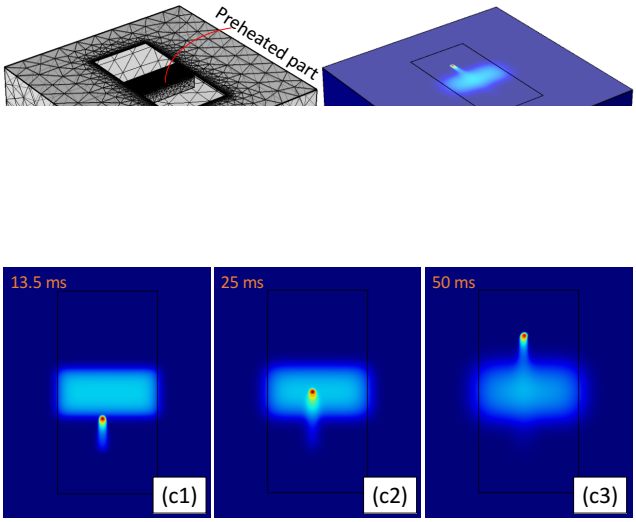

Figure 11: (a): mesh with added preheated part. (The thin layer of powder bed is hidden to unveil the added part.) (b): surface temperature distribution at $t = 49$ ms. (c1)-(c3): surface temperature distributions (top view) during the printing of the first track.

4.2 Periodic Thermal Interactions: In-layer Effects

To investigate the in-layer thermal cycles, we bidirectionally print 10 tracks in the first layer with a hatch spacing of 60 µm (Fig. 6a). Fig. 6b illustrates the simulated surface temperature profile at 0.14 s. From Fig. 10a, we observe that the melt pool width changes over time and structurally deviates from the steady-state value 246 µm as extracted from the first track. Most importantly, the start of each track has larger melt pool widths than the rest of the track. This is because in bidirectional scanning, when the energy beam approaches the end of one track, the large latent heat does not have enough time to dissipate out before the next track starts. The resulting increased melt pool widths at the beginning of each track form a periodic disturbance with a repetitive spectrum in the frequency domain (Fig. 10b). The fundamental frequency f_0 of the disturbance is determined by the duration of scanning one track t_0, that is, $f_0 = 1/t_0 = u_x/L$, where u_x is the scan speed and L is the track length. In this example, $f_0 = 100/5 = 20$ Hz, and frequency spikes at nf_0 ($n \in \mathbb{Z}^+$, the set of positive integers) appear in the fast Fourier transform (FFT) of the disturbance.

The disturbance periodicity is closely related to the recurring laser scanning trajectories and the repetitive in-layer thermomechanical interactions. Besides the bidirectional scan, other scan patterns yield similar repetitive disturbances (see, e.g., experimental results in [33]). To deal with these undesired repetitive spectra, we develop the closed-loop simulation in Section 2 to bring automatic control algorithms [1, 34] into FEM. More results and analyses will be elaborated in Section 5.

4.3 Periodic Thermal Interactions: Combined In- and Cross-layer Effect

This section demonstrates the combined effect of periodic in- and cross-layer thermal interactions. As shown in Fig. 11, we put under the powder bed a Ti6Al4V part ($4.45 \times 1 \times 1\,\text{mm}^3$) that is preheated to 1200 K [35]. Due to the high initial temperature of the added part, the powder on top of the part has a higher initial temperature than the powder elsewhere. The scan strategy is the same as that in Fig. 6a. Eight tracks are scanned bidirectionally with the hatch spacing of 50 µm. The length of the laser track (5 mm) is greater than that of the added part (1 mm). This configuration imitates the printing process of parts with overhang structures, where the preheated Ti6Al4V part corresponds to the previously fused layers. As in Fig. 6, we also use the selective mesh scheme (Fig. 11a): triangular-and-swept (72.6 µm) for the central powder bed, triangular-and-swept (1.5 mm) for the peripheral powder bed, and free tetrahedra (2 mm) for the substrate and the added part.

In Fig. 11, plots (c1)-(c3) illustrate the top views of the surface temperature profiles during the first-track printing from 0 to 50 ms. When the laser is passing over the preheated powder at 25 ms, we get a larger melt pool width, compared to when the laser is approaching ($t = 13.5$ ms) or leaving ($t = 50$ ms) the preheated region. The larger melt pool width is generated due to the higher initial temperature of powder on top of the preheated part.

During the evolution of the melt pool width in Fig. 12a, at the beginning of each track, there is a large increase of the melt pool width caused by the in-layer thermal interaction, as explained in Section 4.2. Besides, as indicated by the arrows in Fig. 12a, larger melt pool widths appear every time the laser passes over the powder on top of the preheated part. These arrowed peaks caused by the cross-layer thermal interaction get smaller as the heat accumulated by the preheated part dissipates out (Tracks 7 and 8 in Fig. 12a). This phenomenon can also be seen from the blurrier border of the preheated region at $t = 50$ ms in Fig. 11 (c3).

We have demonstrated that the periodic evolution of the melt pool width is a lumped output of the repetitive in- and cross-layer heat transfer dynamics. When comparing the frequency spectra in Figs. 10b and 12b, we can tell that the cross-layer thermal interaction changes the magnitudes of the spectral peaks but not the harmonic frequency values. These variations can thus be attenuated by the same feedback control algorithms, such as the RC algorithm to be introduced next.

4.4 RC

RC is designed for tracking/rejecting periodic exogenous references/disturbances in applications with repetitive tasks [36]. By learning from previous iterations, RC can greatly enhance current control performance in the structured task space. Digital RC incorporates an internal model $1/(1 - z^{-N})$ in the controller, where z is the complex indeterminate in the z-transform. $N = f_s/f_0$ is the period of the signal, where $f_s = 1/t_s$ is the sampling frequency and f_0 is

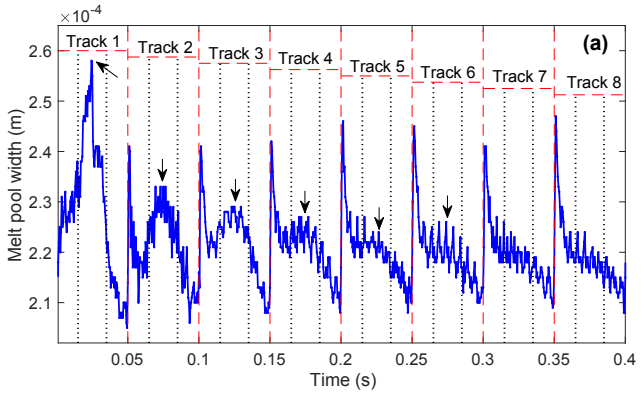

(a) Evolution of melt pool width (time-domain). An interval between two adjacent dashed lines indicates the printing of one track, whereas inside one track, the interval between two adjacent dotted lines denotes when the laser is passing over the preheated part.

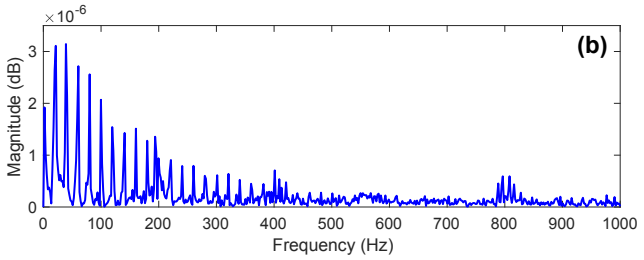

(b) FFT of melt-pool-width evolution (frequency-domain)

Figure 12: Combined in- and cross-layer thermal disturbance.

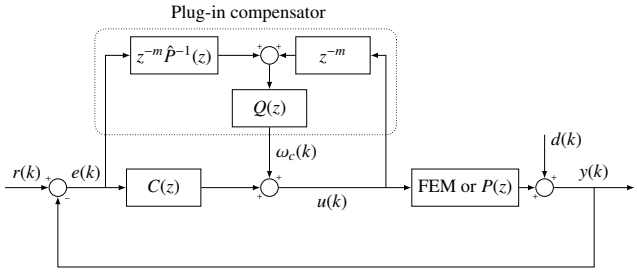

Figure 13: Block diagram of a plug-in RC design.

the fundamental disturbance frequency. Consider a baseline feedback system consisting of $P(z)$ and $C(z)$ (Fig. 2). Here, $C(z)$ can be designed by conventional servo algorithms, such as PID, H_∞, and lead-lag compensation. The sensitivity function $S(z) = \frac{1}{1+P(z)C(z)}$ is the transfer function from $d(k)$ to $y(k)$.

We introduce here a plug-in RC design [34] that uses the internal signals $e(k)$ and $u(k)$ to generate a compensation signal $\omega_c(k)$ (Fig. 13). Let m denote the relative degree of $\hat{P}(z)$, where $\hat{P}(z)$ is the nominal model of $P(z)$. The transfer function of the overall controller from $e(k)$ to $u(k)$ is

$$C_{all}(z) = \frac{C(z) + z^{-m}\hat{P}^{-1}(z)Q(z)}{1 - z^{-m}Q(z)}. \tag{5}$$

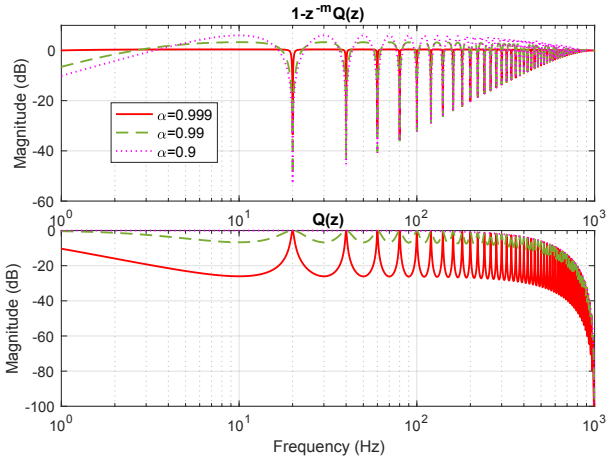

Figure 14: Magnitude responses of $1-z^{-m}Q(z)$ and $Q(z)$ with different values of α (and $n_0 = 1$) in an example of Section 5.

The internal model is integrated in C_{all} by designing the Q filter as $Q(z) = (1-\alpha^N)z^{m-N}/(1-\alpha^N z^{-N})$, which gives $1 - z^{-m}Q(z) = (1-z^{-N})/(1-\alpha^N z^{-N})$. Here, $\alpha \in [0, 1)$ is a tuning factor that determines the attenuation width of $1 - z^{-m}Q(z)$. At the harmonic frequencies $\omega_k = k2\pi f_0 t_s$ ($k \in \mathbb{Z}^+$), with $z = e^{j\omega_k}$, we have $1 - z^{-N} = 0$, $1 - z^{-m}Q(z) = 0$, $C_{all}(z) \to \infty$ from (5), and hence the new sensitivity function $S_0(z) = \frac{1}{1+P(z)C_{all}(z)} = 0$. At the intermediate frequencies $\omega \neq k2\pi f_0 t_s$, with $z = e^{j\omega}$ and α being close to 1, $Q(z) \approx 0$, $1 - z^{-m}Q(z) \approx 1$, $C_{all}(z) \approx C(z)$ from (5), and thereby the original loop shape is maintained. A smaller α can yield a wider attenuation width at the cost of deviating from the baseline loop shape, as shown in Fig. 14.

During implementation, a zero-phase low-pass filter $q_0(z^{-1})q_0(z)$ is attached to $Q(z)$ for robustness against high-frequency plant uncertainties:

$$Q(z) = \frac{(1-\alpha^N)z^{m-N}}{1-\alpha^N z^{-N}} q_0(z^{-1})q_0(z), \tag{6}$$

where $q_0(z) = (1+z)^{n_0}/2^{n_0}$ and $n_0 \in \mathbb{Z}^+$ (Fig. 15). The closed-loop performance $S_0(z)$ can be tuned by choosing different α and n_0 [34]. The plug-in RC and the baseline control can be merged into the closed-loop simulation by setting $u(k)$ as $q(t_f)$ and $y(k)$ as $w(t_f)$ (see Fig. 3).

5 Results and Analyses

Under the infrastructure of the closed-loop simulation, we evaluate the performance of RC in attenuating the periodic in-layer variations of the melt pool width.

First, we identify the plant model of the FEM in Section 3 from the laser power to the melt pool width as $P(s) = 0.001671/(s+1055)$. The input signals used for system identification include a pseudorandom binary sequence (PRBS) signal and multiple sinusoidal signals (10~300 Hz), with magnitudes of 20 W and add-on DC components of 60 W. The frequency responses of the measured and identified systems match well with each other, as shown in Fig. 16.

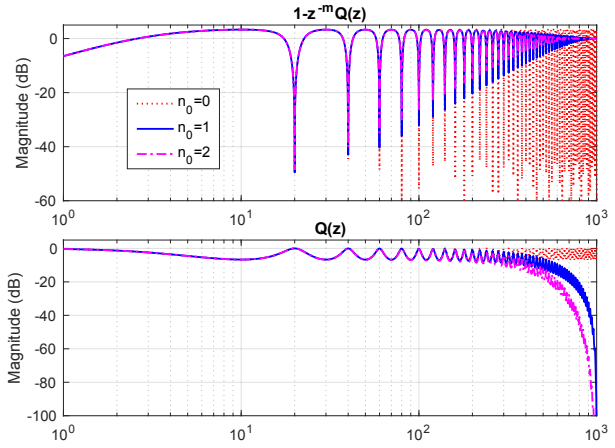

Figure 15: Magnitude responses of $1-z^{-m}Q(z)$ and $Q(z)$ wit different n_0 (and $\alpha = 0.99$) in an example of Section 5.

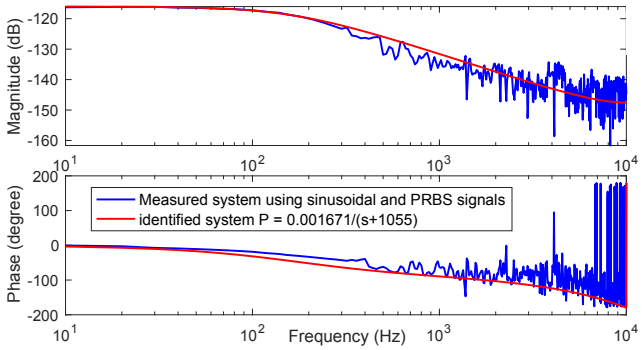

Figure 16: Measured and identified system responses.

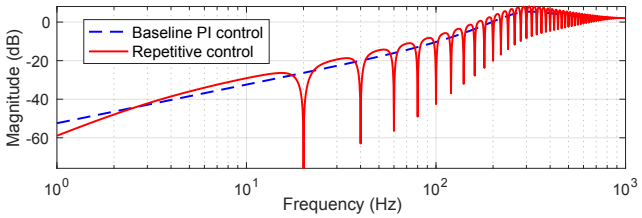

Figure 17: Magnitude responses of sensitivity functions $S(z)$ in baseline control and $S_0(z)$ in RC.

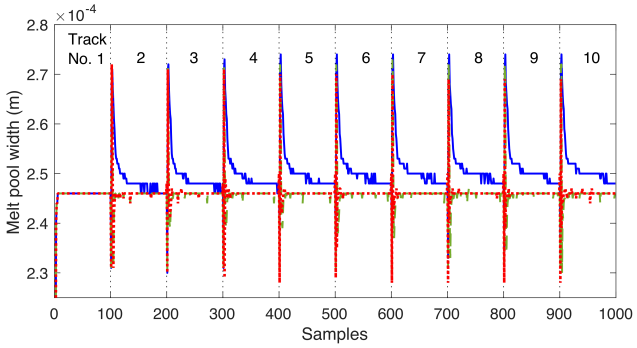

(a) Evolution of melt pool width (time-domain)

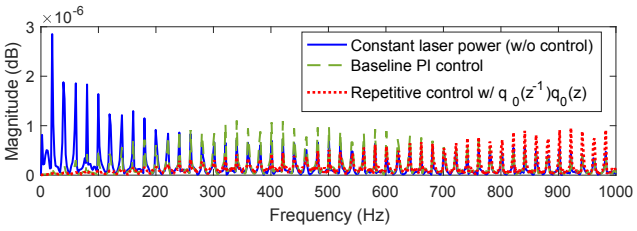

(b) FFT of melt-pool-width evolution (frequency-domain)

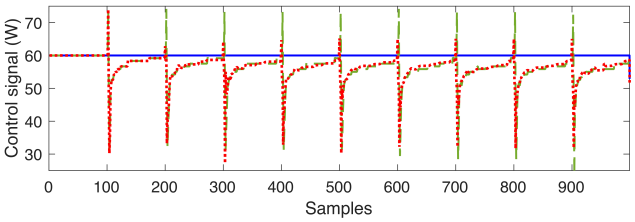

(c) Laser power (control signals $u(k)$ in Fig. 13)

Figure 18: In-layer thermal disturbance. The three plots share the same legend. The 3σ-values of the melt pool width respectively are 15.219 µm for constant laser power, 11.937 µm (21.6% decrease) for baseline PI control, and 9.744 µm (35.97% decrease) for RC. σ denotes the standard deviation. The earlier results in Fig. 10 are superimposed in Figs. 18a and 18b for clarity.

After that, we design a PI controller as $C(s) = K_p + K_i/s$ with $K_p = 9.38\times10^5$ and $K_i = 1.66\times10^9$. Under the sampling time t_s of 0.5 ms (i.e., $f_s = 2$ kHz), the zero-order-hold equivalents of the plant and controller models respectively are $P(z) = 6.493\times10^{-7}/(z-0.5901)$ and $C(z) = (9.38z-1.08)\times10^5/(z-1)$. The dashed line in Fig. 17 shows the magnitude response of the sensitivity function $S(z)$ in the baseline feedback loop that comprises $P(z)$ and $C(z)$. Such a design provides a bandwidth at 197 Hz, which approximates the limit of 20% of the Nyquist frequency (1000 Hz) and indicates that the PI controller is well tuned. The closed-loop simulations are designed according to Section 3 integrating FEM with baseline control and RC, respectively. In this disturbance-rejection example, $r(k) = 0$ in Fig. 13, and $d(k)$ comes from the in-layer melt-pool-width variations (Section 4.2). From Fig. 18b, we can tell that the baseline PI control can attenuate the frequency spikes below the closed-loop bandwidth but not the other high-frequency spikes. Compared to the case without control, the baseline feedback loop decreases the 3σ value of the melt-pool-width changes ($y(k)$ in Fig. 13 with mean removed) by 21.57%, where σ denotes the standard deviation.

To enhance the disturbance-attenuation performance, we bring the plug-in RC compensator in Section 4.4 into the closed-loop high-fidelity simulation. In the Q-filter design in (6), the relative degree m of $\hat{P}(z)$ is 1 with $\hat{P}(z)$ being equal to $P(z)$ in this simulation example; the disturbance period $N = f_s/f_0 = 2000/20 = 100$; we choose $\alpha = 0.99$. Also, we attach a low-pass filter with $n_0 = 1$ to $Q(z)$ as in (6). As shown in the solid line of Fig. 17, the plug-in RC with the Q-filter generates high-gain control efforts exactly at 20 Hz and its harmonics. Fig. 18c illustrates the control signals $u(k)$ of

the baseline control, the RC, and the case without control. As shown in Fig. 18b, compared with the baseline control, RC further lowers the periodic frequency spikes, especially at high frequencies beyond the closed-loop bandwidth, and decreases the 3σ value by 35.97%. Similarly, in the time domain, the increased control efforts of RC at the harmonic frequencies yield a further-attenuated output $y(k)$, as shown in Fig. 18a.

Remark 1: Practical feedback design has an effective servo bandwidth, above which the control efforts are required to be small for robustness. The baseline PI control and the Q-filter with $q_0(z^{-1})q_0(z)$ are designed to account for this constraint. As shown in Fig. 17, above approximately 650 Hz, the magnitudes of the sensitivity functions of baseline PI control and RC are close to zero, leaving the corresponding frequency components unchanged.

Remark 2: To compute the closed-loop simulation with the FEM in Section 3, it takes approximately 19 seconds for one time step of 0.5 ms, 32 minutes for a track of length 5 mm, and 4.5 hours for ten tracks of length 5 mm using two Intel Xeon Gold 6146 CPUs at 3.20 GHz with 24 cores in total.

6 Conclusions and Future Work

In this paper, we develop a first-instance closed-loop high-fidelity simulation architecture by integrating finite element model (FEM) with feedback controls to reduce the in-process variations and advance the part quality in powder bed fusion (PBF) additive manufacturing. We build an FEM to simulate the temperature response in PBF and then validate the FEM by comparing its results with the experimental and analytical solutions. Employing the FEM, we justify the existence of the periodic disturbances in the evolution of the melt pool width. From there, implementing the proposed closed-loop simulation, we validate that the repetitive control algorithm attenuates the periodic disturbances more substantially by 35.97% than the PI control.

One avenue for future work is to expand the proposed closed-loop simulation to be used in multi-layer printing when macroscopic features begin to form. The proposed architecture enables simulating in the FEM the development of the macroscopic temperature history and the melt pool geometries under the influence of feedback controls. To relieve the computation burden incurred by the high-fidelity simulation of multiple layers, we can start with a thin-wall build with small numbers of tracks (say one or two) within one layer.

Acknowledgements

This material is based upon work supported in part by the National Science Foundation under Grant No. 1953155. We would like to thank all the reviewers and editors for their insightful comments and great efforts towards improving this manuscript.

Appendix: main MATLAB commands in the proposed closed-loop simulation

```
% Importing the COMSOL classes
import com.comsol.model.*
import com.comsol.model.util.*

% Open COMSOL mph file
model = mphopen('FEM_file_with_one_time_step');
ht = model.physics('ht');

% Compute FEM
model.study('std1').run;

% Get the whole temperature distribution
[x0, y0, T, tt] = mphinterp(model, {'x',…
   'y', 'T', 't'}, 'coord', coord, 't', t);

% Set tf to t0
time = mphglobal(model,'t','solnum','end');
model.param.set('t0', time);

% Set T(tf) to T(t0)
ht.feature('init1').set('T', 'T');
v1 = model.sol('sol1').feature('v1');
v1.set('initsol', 'sol1');

% Set q(tf) to q
model.param.set('laserpower', q);
```

References

[1] D. Wang and X. Chen, "A multirate fractional-order repetitive control for laser-based additive manufacturing," *Control Engineering Practice*, vol. 77, pp. 41–51, 2018.

[2] J.-P. Kruth, P. Mercelis, J. Van Vaerenbergh, and T. Craeghs, "Feedback control of selective laser melting," in *Proceedings of the 3rd international conference on advanced research in virtual and rapid prototyping*, 2007, pp. 521–527.

[3] V. Seyda, N. Kaufmann, and C. Emmelmann, "Investigation of aging processes of ti-6al-4 v powder material in laser melting," *Physics Procedia*, vol. 39, pp. 425–431, 2012.

[4] M. Masoomi, S. M. Thompson, and N. Shamsaei, "Laser powder bed fusion of ti-6al-4v parts: Thermal modeling and mechanical implications," *International Journal of Machine Tools and Manufacture*, vol. 118, pp. 73–90, 2017.

[5] A. Hussein, L. Hao, C. Yan, and R. Everson, "Finite element simulation of the temperature and stress fields in single layers built without-support in selective laser melting," *Materials & Design (1980-2015)*, vol. 52, pp. 638–647, 2013.

[6] A. Foroozmehr, M. Badrossamay, E. Foroozmehr, and S. Golabi, "Finite element simulation of selective laser melting process considering optical penetration depth of laser in powder bed," *Materials & Design*, vol. 89, pp. 255–263, 2016.

[7] S. A. Khairallah, A. T. Anderson, A. Rubenchik, and W. E. King, "Laser powder-bed fusion additive manufacturing: Physics of complex melt flow and formation mechanisms of pores, spatter, and denudation zones," *Acta Materialia*, vol. 108, pp. 36–45, 2016.

[8] T. Debroy, W. Zhang, J. Turner, and S. S. Babu, "Build-

ing digital twins of 3d printing machines," *Scripta Materialia*, vol. 135, pp. 119–124, 2017.

[9] T. Craeghs, F. Bechmann, S. Berumen, and J.-P. Kruth, "Feedback control of layerwise laser melting using optical sensors," *Physics Procedia*, vol. 5, pp. 505–514, 2010.

[10] C. Zheng, J. T. Wen, and M. Diagne, "Distributed temperature control in laser-based manufacturing," *Journal of Dynamic Systems, Measurement, and Control*, vol. 142, no. 6, 2020.

[11] L. Song and J. Mazumder, "Feedback control of melt pool temperature during laser cladding process," *IEEE Transactions on Control Systems Technology*, vol. 19, no. 6, pp. 1349–1356, 2011.

[12] X. Cao and B. Ayalew, "Control-oriented mimo modeling of laser-aided powder deposition processes," in *American Control Conference (ACC), 2015*. IEEE, 2015, pp. 3637–3642.

[13] P. M. Sammons, D. A. Bristow, and R. G. Landers, "Repetitive process control of laser metal deposition," in *ASME 2014 Dynamic Systems and Control Conference*. American Society of Mechanical Engineers, 2014, pp. V002T35A004–V002T35A004.

[14] A. Fathi, A. Khajepour, M. Durali, and E. Toyserkani, "Geometry control of the deposited layer in a nonplanar laser cladding process using a variable structure controller," *Journal of manufacturing science and engineering*, vol. 130, no. 3, p. 031003, 2008.

[15] M. L. Vlasea, B. Lane, F. Lopez, S. Mekhontsev, and A. Donmez, "Development of powder bed fusion additive manufacturing test bed for enhanced real-time process control," in *Proceedings of the international solid freeform fabrication symposium, Austin, TX, USA*, 2015, pp. 13–15.

[16] T. G. Fleming, S. G. Nestor, T. R. Allen, M. A. Boukhaled, N. J. Smith, and J. M. Fraser, "Tracking and controlling the morphology evolution of 3d powder-bed fusion in situ using inline coherent imaging," *Additive Manufacturing*, vol. 32, p. 100978, 2020.

[17] J. Hofman, B. Pathiraj, J. Van Dijk, D. de Lange, and J. Meijer, "A camera based feedback control strategy for the laser cladding process," *Journal of Materials Processing Technology*, vol. 212, no. 11, pp. 2455–2462, 2012.

[18] D. Salehi and M. Brandt, "Melt pool temperature control using labview in nd: Yag laser blown powder cladding process," *The international journal of advanced manufacturing technology*, vol. 29, no. 3, pp. 273–278, 2006.

[19] A. Fathi, A. Khajepour, E. Toyserkani, and M. Durali, "Clad height control in laser solid freeform fabrication using a feedforward pid controller," *The International Journal of Advanced Manufacturing Technology*, vol. 35, no. 3, pp. 280–292, 2007.

[20] L. Tang and R. G. Landers, "Layer-to-layer height control for laser metal deposition process," *Journal of Manufacturing Science and Engineering*, vol. 133, no. 2, p. 021009, 2011.

[21] Z. Luo and Y. Zhao, "A survey of finite element analysis of temperature and thermal stress fields in powder bed fusion additive manufacturing," *Additive Manufacturing*, vol. 21, pp. 318–332, 2018.

[22] T. Mukherjee, H. Wei, A. De, and T. DebRoy, "Heat and fluid flow in additive manufacturing—part i: Modeling of powder bed fusion," *Computational Materials Science*, vol. 150, pp. 304–313, 2018.

[23] E. Kannatey-Asibu Jr, *Principles of laser materials processing*. John Wiley & Sons, 2009, vol. 4.

[24] A. N. Arce, *Thermal modeling and simulation of electron beam melting for rapid prototyping on Ti6Al4V alloys*. North Carolina State University, 2012.

[25] K. Karayagiz, A. Elwany, G. Tapia, B. Franco, L. Johnson, J. Ma, I. Karaman, and R. Arróyave, "Numerical and experimental analysis of heat distribution in the laser powder bed fusion of ti-6al-4v," *IISE Transactions*, vol. 51, no. 2, pp. 136–152, 2019.

[26] J. Yin, H. Zhu, L. Ke, W. Lei, C. Dai, and D. Zuo, "Simulation of temperature distribution in single metallic powder layer for laser micro-sintering," *Computational Materials Science*, vol. 53, no. 1, pp. 333–339, 2012.

[27] I. Yadroitsev, *Selective laser melting: Direct manufacturing of 3D-objects by selective laser melting of metal powders*. LAP LAMBERT Academic Publishing, 09 2009.

[28] I. Yadroitsev, P. Krakhmalev, and I. Yadroitsava, "Selective laser melting of ti6al4v alloy for biomedical applications: Temperature monitoring and microstructural evolution," *Journal of Alloys and Compounds*, vol. 583, pp. 404–409, 2014.

[29] K. C. Mills, *Recommended values of thermophysical properties for selected commercial alloys*. Woodhead Publishing, 2002.

[30] C. Cepeda-Jiménez, F. Potenza, E. Magalini, V. Luchin, A. Molinari, and M. Pérez-Prado, "Effect of energy density on the microstructure and texture evolution of ti-6al-4v manufactured by laser powder bed fusion," *Materials Characterization*, p. 110238, 2020.

[31] L. Thijs, F. Verhaeghe, T. Craeghs, J. Van Humbeeck, and J.-P. Kruth, "A study of the microstructural evolution during selective laser melting of ti–6al–4v," *Acta materialia*, vol. 58, no. 9, pp. 3303–3312, 2010.

[32] T. Majumdar, T. Bazin, E. Massahud Carvalho Ribeiro, J. E. Frith, and N. Birbilis, "Understanding the effects of pbf process parameter interplay on ti-6al-4v surface properties," *PloS one*, vol. 14, no. 8, p. e0221198, 2019.

[33] A. J. Dunbar, E. R. Denlinger, M. F. Gouge, T. W. Simpson, and P. Michaleris, "Comparisons of laser powder bed fusion additive manufacturing builds through experimental in situ distortion and temperature measurements," *Additive Manufacturing*, vol. 15, pp. 57–65, 2017.

[34] X. Chen and M. Tomizuka, "New repetitive control with improved steady-state performance and accelerated transient," *IEEE Transactions on Control Systems Technology*, vol. 22, no. 2, pp. 664–675, 2014.

[35] S. Liu and Y. C. Shin, "Additive manufacturing of ti6al4v alloy: A review," *Materials & Design*, vol. 164, p. 107552, 2019.

[36] T. Inoue, M. Nakano, T. Kubo, S. Matsumoto, and H. Baba, "High accuracy control of a proton synchrotron magnet power supply," *IFAC Proceedings Volumes*, vol. 14, no. 2, pp. 3137–3142, 1981.